ACS APPLIED OPTICAL MATERIALS

pubs.acs.org/acsaom Article

Anisotropic Raman Response from Isotropic Constituents in BP/MoS_2 Heterostructures

Published as part of ACS Applied Optical Materials special issue "100 Years of Raman Effect: Celebrating a Century of Molecular Insight and Shaping the Future".

Zi-Han Zhang,[▽] Chen-Kai Liu,[▽] Jia-Liang Xie, Rui Mei, Tao Liu, Miao-Ling Lin, and Ping-Heng Tan*

Cite This: ACS Appl. Opt. Mater. 2025, 3, 2655−2661 Read Online

ACCESS | Metrics & More | Article Recommendations | Supporting Information

ABSTRACT: Anisotropic layered materials (ALMs) can be integrated with isotropic materials to form van der Waals heterostructures (vdWHs) for polarization-sensitive optoelectronic applications, yet the influence of ALM optical anisotropy on the Raman response of isotropic components remains an open question. This study demonstrates that monolayer MoS_2 in black phosphorus/MoS_2 (BP/1LM) vdWHs exhibits pronounced in-plane anisotropic Raman responses despite its intrinsic isotropy, as revealed through angle-resolved polarized Raman (ARPR) spectroscopy. The A_1' and E' mode intensities of the 1LM constituent display strong angular dependencies that closely mimic the anisotropic profiles of the Raman modes of BP, resulting from the birefringence and linear dichroism of BP combined with interference effects within the multilayer stack. The theoretical calculations incorporating depth-dependent field modulation and multilayer interference reproduce the experimental results and demonstrate dependence on the BP thickness and excitation wavelength. This work provides a quantitative framework for understanding and engineering optical anisotropy in heterostructures comprising isotropic and anisotropic two-dimensional materials.

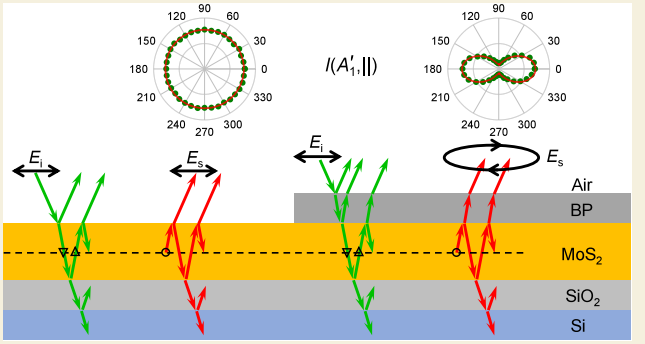

KEYWORDS: *angle-resolved polarized Raman, anisotropic materials, van der Waals heterostructures, birefringence, linear dichroism, interference effects*

INTRODUCTION

Black phosphorus (BP), a prototypical anisotropic layered material (ALM), exhibits in-plane anisotropy in its electrical, thermal, and optical properties due to its unique puckered honeycomb structure.[1−3] Its layer-dependent bandgap (tunable from ∼0.3 eV in bulk to ∼2 eV in monolayers) bridges the gap between zero-bandgap graphene and large-bandgap transition metal dichalcogenides (TMDs), making BP promising for polarization-sensitive photodetectors,[4] field effect transistors,[5] and thermoelectric devices.[6] Angle-resolved polarized Raman (ARPR) spectroscopy[7,8] has been widely used to study ALMs, probing their lattice symmetry,[9,10] optical anisotropy,[7−9,11−13] electron−phonon interactions,[8,14,15] crystalline orientation,[16] and edge effects.[17,18] In the standard backscattering configuration, the Raman intensity I of a phonon mode follows the selection rule $I \propto |\boldsymbol{e}_s^T \cdot \boldsymbol{R} \cdot \boldsymbol{e}_i|^2$, where $\boldsymbol{e}_i$ and $\boldsymbol{e}_s$ represent the polarization vectors of the incident and scattered light outside the crystal, $\boldsymbol{e}_s^T$ is the transpose of $\boldsymbol{e}_s$, and $\boldsymbol{R}$ denotes the Raman tensor.[19] Although the tensor elements of $\boldsymbol{R}$ in optically isotropic crystals (e.g., cubic structures) may be complex quantities, only their magnitudes contribute to I due to the absence of birefringence and dichroism. However, ALMs require consideration of both magnitude and phase components in $\boldsymbol{R}$ to accurately fit ARPR intensity due to their inherent anisotropy.[7−9,11] Birefringence and linear dichroism in ALMs introduce depth-dependent polarization and amplitude variations in both excitation and scattered fields, meaning that $\boldsymbol{e}_i$ and $\boldsymbol{e}_s$ at the scattering site cannot be treated as constants.[8,12] For near-normal incidence on the basal plane, effective Raman tensors $\boldsymbol{R}^{eff}$, which are directly linked to $\boldsymbol{e}_i$ and $\boldsymbol{e}_s$, can be derived from intrinsic Raman tensors $\boldsymbol{R}^{int}$ by considering birefringence, linear dichroism, and multilayer interference inside multilayered structures.[8] This approach enables the quantitative modeling of ARPR intensity profiles in ALMs.[8]

Received: August 25, 2025
Revised: October 18, 2025
Accepted: October 19, 2025
Published: October 28, 2025

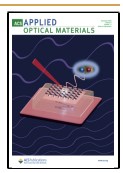

https://doi.org/10.1021/acsaom.5c00385
ACS Appl. Opt. Mater. 2025, 3, 2655−2661

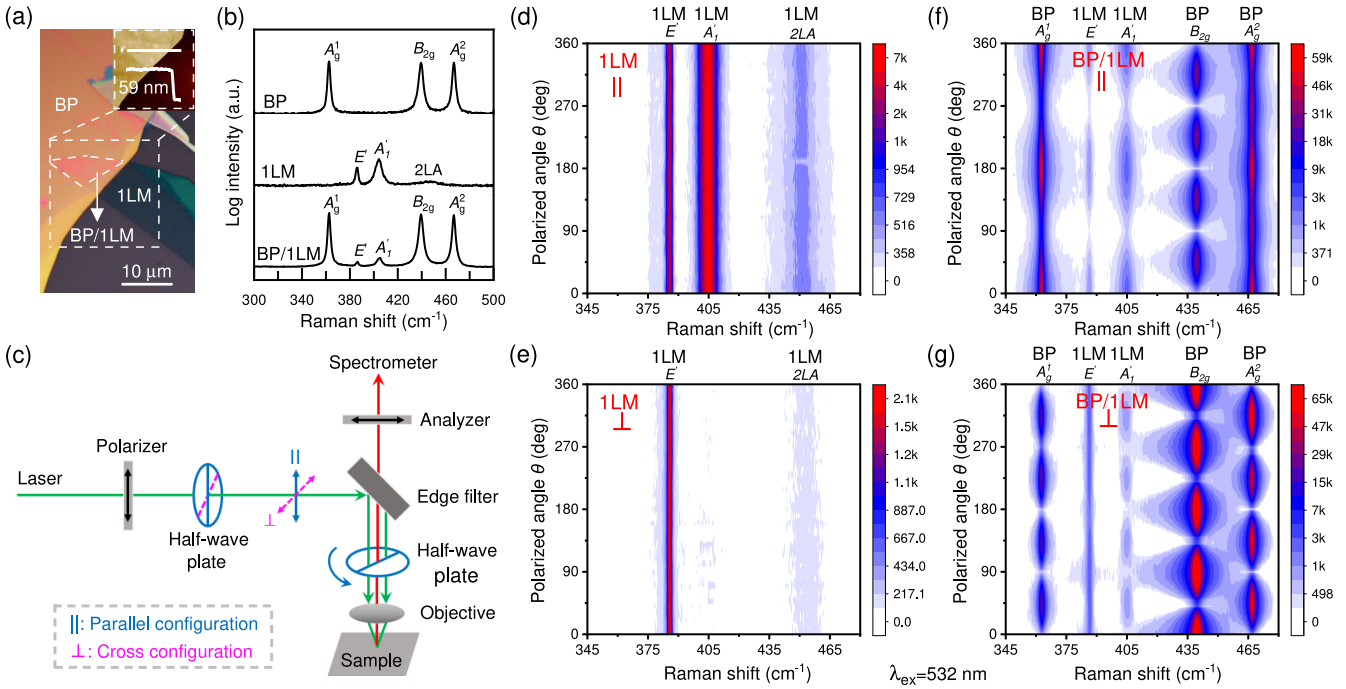

Figure 1. (a) Optical image of a 59 nm-BP/1LM and AFM image (inset) of the 59 nm BP flake; (b) Raman spectra of BP, 1LM, and BP/1LM excited by λ_{ex} = 532 nm; (c) schematic diagram of ARPR spectroscopy setup with parallel and cross-polarization configurations; ARPR spectra of (d, e) 1LM and (f, g) BP/1LM under (d, f) parallel and (e, g) cross-polarization configurations, respectively.

For polarization-sensitive electronic and optoelectronic applications, anisotropic layered materials (ALMs) are often integrated with isotropic 2D materials (2DMs), such as TMDs, graphene, and hBN, to form van der Waals heterostructures (vdWHs).[20,21] Examples include BP/MoS_2,[22−25] BP/WSe_2,[20,26,27] and BP/Bi_2Se_3.[28] Due to birefringence, linear dichroism in the ALM component, and multilayer interference effects, the excitation and scattered electric fields in the isotropic 2DM exhibit a complex anisotropic optical response, similar to that of ALMs.[28] This response is expected to depend on the thickness of the ALM constituent. While anisotropic optical behavior has been briefly observed in a few isotropic constituents of ALM-based vdWHs,[28] a quantitative understanding of their ARPR intensity profiles remains an open challenge in the field.

In this work, we investigate the anisotropic optical response of isotropic constituents in ALM-based vdWHs through systematic studies of BP/MoS_2 systems. We prepared BP-based vdWHs incorporating monolayer MoS_2 (1LM) on 90 nm-SiO_2/Si substrates, employing ARPR spectroscopy at excitation wavelengths (λ_{ex}) of 532 and 488 nm. Building upon established ARPR intensity models for thick BP flakes,[8] we developed a theoretical framework that accounts for birefringence, linear dichroism, and multilayer interference effects in BP/1LM/substrate multilayer structures. Our model successfully reproduces the experimental ARPR intensity profiles of the 1LM constituent for various BP thicknesses (d_{BP}), quantitatively demonstrating how the anisotropic BP layer fundamentally alters the optical response of the isotropic monolayer.

METHODS

Sample Preparation

1LM and BP flakes were mechanically exfoliated from bulk crystals onto PDMS substrates. Using an all-dry viscoelastic stamping method,[29] we fabricated BP/1LM vdWHs by sequentially transferring flakes onto 90 nm-SiO_2/Si substrates under optical microscopy guidance with a nanomanipulator. The typical optical image of a BP/1LM vdWH is illustrated in Figure 1a. 1LM was confirmed through the frequency difference of 19.1 cm^{-1} between its A_1' and E' Raman modes[30] (Figure 1b). d_{BP} was precisely determined by atomic force microscopy in tapping mode.

Raman Measurements

Raman spectra were acquired in backscattering geometry at room temperature using an HR-Evolution micro-Raman system featuring a liquid-nitrogen-cooled charge-coupled device (CCD) and a 50× objective (numerical aperture = 0.35), with λ_{ex} of 488 nm (Ar^+ laser) and 532 nm (solid-state laser). The ARPR measurement setup (Figure 1c) employed a vertically aligned polarizer and analyzer, with a half-wave plate (HWP) downstream of the polarizer enabling parallel/cross-polarization configurations and another rotatable half-wave plate in the common optical path for ARPR spectra acquisition. A proper HWP with a small retardance error is selected to obtain reliable results of ARPR spectroscopy for ALM-based vdWHs.[31] The laser power was kept below 0.5 mW to avoid sample heating, and measurements were conducted in a vacuum chamber to prevent sample degradation.

Computational Methods

As presented in Figure 1c, both polarization vectors $\boldsymbol{e}_i$ and $\boldsymbol{e}_s$ are controlled by the half-wave plate in the common optical path. For the parallel polarization configuration, $\boldsymbol{e}_i = \boldsymbol{e}_s = (\cos\theta, \sin\theta, 0)^T$, where θ refers to twice the angle of the HWP fast axis with respect to the x-axis. In contrast, in the cross-polarization configuration, $\boldsymbol{e}_i = (-\sin\theta, \cos\theta, 0)^T$ and $\boldsymbol{e}_s = (\cos\theta, \sin\theta, 0)^T$, respectively.

For the BP/1LM deposited on the SiO_2/Si substrate, a five-layer structure can be established, containing air ($\tilde{n}_0$), BP ($\tilde{n}_1$, d_1), 1LM ($\tilde{n}_2$, d_2), SiO_2 ($\tilde{n}_3$, d_3) and Si ($\tilde{n}_4$), where $\tilde{n}_\mu$ (μ = 0, 1, 2, 3, 4) and d_μ (μ = 1, 2, 3) are the complex refractive index and the thickness of each medium, as illustrated in Figure 2a. The x- and y-axes were established in alignment with the in-plane zigzag (ZZ) and armchair (AC) directions of the BP constituent, respectively. $\tilde{n}_\mu$ of each medium can be extracted from previous literature (see Supporting Information Table S1 for details).[8,32,33] At near-normal incidence, the propagation

https://doi.org/10.1021/acsaom.5c00385
ACS Appl. Opt. Mater. 2025, 3, 2655−2661

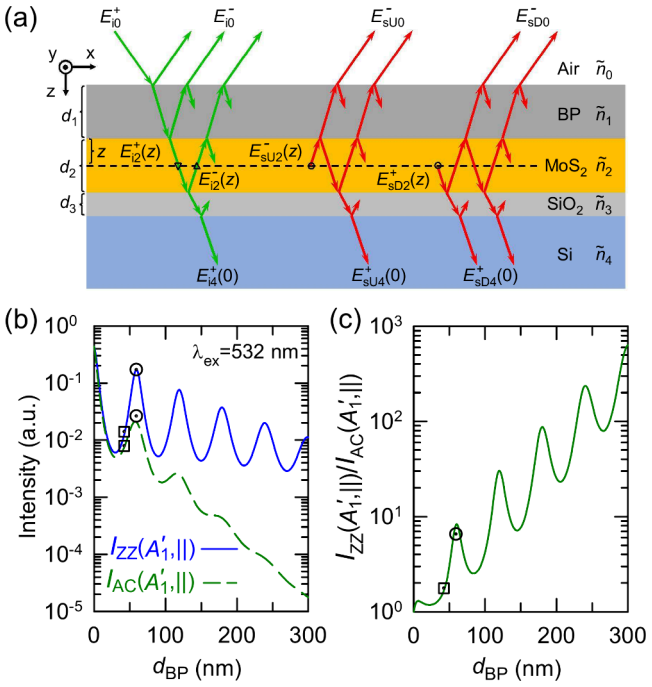

Figure 2. (a) Schematic diagram of the multilayer interference of incident light and Raman-scattered light within the multilayered dielectric structure of air/BP/1LM/90 nm-SiO_2/Si (oblique incidence and scattering for convenience). (b) $I_{ZZ}(A_1', \|)$, $I_{AC}(A_1', \|)$, and (c) $I_{ZZ}(A_1', \|)/I_{AC}(A_1', \|)$ of the 1LM constituent in BP/1LM deposited on 90 nm-SiO_2/Si substrate as a function of d_{BP}, λ_{ex} = 532 nm. Open circles and squares denote normalized Raman intensities of the 1LM component in 59 nm-BP/1LM and 42 nm-BP/1LM heterostructures, respectively.

of the incident light in the BP constituent aligns with the z-axis. The electric field of light propagating perpendicular to the basal plane of the BP constituent can be decomposed into two orthogonal polarization components along the ZZ and AC directions. Accordingly, $\tilde{n}_1$ can be decomposed into $\tilde{n}_{ZZ} = n_{ZZ} + i\kappa_{ZZ}$ and $\tilde{n}_{AC} = n_{AC} + i\kappa_{AC}$, where n and κ represent the refractive index and extinction coefficient of the BP constituent, respectively, and i is the imaginary unit. In the air/BP/1LM/substrate dielectric multilayer, the electric fields of both the incident light and Raman-scattered light from the 1LM constituent are modified by birefringence and linear dichroism of the BP constituent and the multilayer interference effect inside multilayered structures. Building upon established ARPR intensity models for thick BP flakes,[8] these modulations can be quantified by the interference factor matrices $\boldsymbol{F}_{i(s)}(z)$ of

$$\boldsymbol{F}_{i(s)}(z) = \begin{pmatrix} F_{i(s)}^{ZZ}(z) & 0 & 0 \\ 0 & F_{i(s)}^{AC}(z) & 0 \\ 0 & 0 & 1 \end{pmatrix} \tag{1}$$

in which $F_{i(s)}^{ZZ}(z)$ and $F_{i(s)}^{AC}(z)$ are, respectively, the enhancement factors corresponding to the 1LM constituent at the location of the scattering event for the incident (or Raman-scattered) light along the ZZ and AC directions of the BP constituent.[8] Equation 1 can be calculated by the transfer matrix method (see eqs S1-S12 in the Supporting Information for details) based on the birefringence and linear dichroism of the BP constituent and multilayer interference effect in the air/BP/1LM/substrate multilayer system.[8] Since Raman scattering occurs within the 1LM constituent, the measured I for the A_1' and E' modes from the 1LM constituent is, respectively, given by

$$I(A_1') \propto \int_0^{d_2} |\boldsymbol{e}_s^{\mathrm{T}} \boldsymbol{F}_s^{\mathrm{T}}(z) \cdot \boldsymbol{R}(A_1') \cdot \boldsymbol{F}_i(z) \boldsymbol{e}_i|^2 \, dz \tag{2}$$

$$I(E') \propto \sum_{j=1}^{2} \int_0^{d_2} |\boldsymbol{e}_s^{\mathrm{T}} \boldsymbol{F}_s^{\mathrm{T}}(z) \cdot \boldsymbol{R}_j(E') \cdot \boldsymbol{F}_i(z) \boldsymbol{e}_i|^2 \, dz \tag{3}$$

where j is the subscript of Raman tensors for the doubly degenerate E' modes. Due to its in-plane optical isotropy, the Raman tensor $\boldsymbol{R}$ of 1LM does not require differentiation between its intrinsic form $\boldsymbol{R}^{int}$ and effective form $\boldsymbol{R}^{eff}$, with the tensors for the A_1' and E' modes explicitly given as follows:[30]

$$\boldsymbol{R}^{int}(A_1') = \begin{pmatrix} a & 0 & 0 \\ 0 & a & 0 \\ 0 & 0 & b \end{pmatrix} \tag{4}$$

$$\boldsymbol{R}_1^{int}(E') = \begin{pmatrix} 0 & d & 0 \\ d & 0 & 0 \\ 0 & 0 & 0 \end{pmatrix}, \boldsymbol{R}_2^{int}(E') = \begin{pmatrix} d & 0 & 0 \\ 0 & -d & 0 \\ 0 & 0 & 0 \end{pmatrix} \tag{5}$$

The tensor elements a, b, and d can be expressed in complex form as $a = |a|e^{i\phi_a}$, $b = |b|e^{i\phi_b}$, and $d = |d|e^{i\phi_d}$, where $|a|$, $|b|$, and $|d|$ represent the amplitudes while ϕ_a, ϕ_b, and ϕ_d correspond to their respective phase components.[7,8]

By substituting the Raman tensors (eqs 4 and 5) of 1LM into eqs 2 and 3, the angle-dependent $I(A_1')$ and $I(E')$ of the 1LM constituent in the BP/1LM under the parallel polarization ($\|$) and cross-polarization ($\perp$) configurations are given as follows:

$$I(A_1', \|, \theta) \propto |a|^2 \int_0^{d_2} |F_i^{ZZ} F_s^{ZZ} \cos^2\theta + F_i^{AC} F_s^{AC} \sin^2\theta|^2 \, dz \tag{6}$$

$$I(E', \|, \theta) \propto |d|^2 \int_0^{d_2} \left(\frac{1}{4} |F_i^{AC} F_s^{ZZ} + F_i^{ZZ} F_s^{AC}|^2 \sin^2 2\theta + |F_i^{ZZ} F_s^{ZZ} \cos^2\theta - F_i^{AC} F_s^{AC} \sin^2\theta|^2 \right) dz \tag{7}$$

$$I(A_1', \perp, \theta) \propto |a|^2 \int_0^{d_2} \frac{1}{4} |-F_i^{ZZ} F_s^{ZZ} + F_i^{AC} F_s^{AC}|^2 \sin^2 2\theta \, dz \tag{8}$$

$$I(E', \perp, \theta) \propto |d|^2 \int_0^{d_2} \left(\frac{1}{4} |-F_i^{ZZ} F_s^{ZZ} - F_i^{AC} F_s^{AC}|^2 \sin^2 2\theta + |F_i^{AC} F_s^{ZZ} \cos^2\theta - F_i^{ZZ} F_s^{AC} \sin^2\theta|^2 \right) dz \tag{9}$$

Under parallel polarization (θ = 0°, i.e., $\boldsymbol{e}_i \| \boldsymbol{e}_s \|$ZZ), the Raman intensities for A_1' and E' are denoted as $I_{ZZ}(A_1', \|)$ and $I_{ZZ}(E', \|)$, respectively, whereas for θ = 90° ($\boldsymbol{e}_i \| \boldsymbol{e}_s \|$AC), they become $I_{AC}(A_1', \|)$ and $I_{AC}(E', \|)$. Similarly, under cross-polarization, the corresponding intensities are expressed as $I_{ZZ}(A_1', \perp)$, $I_{ZZ}(E', \perp)$, $I_{AC}(A_1', \perp)$, and $I_{AC}(E', \perp)$.

Equations 6–9 explicitly demonstrate how the optical anisotropy of the BP constituent within BP/1LM transforms the ARPR intensity profiles of intrinsically isotropic Raman modes of the corresponding 1LM constituent into an anisotropic form, and in the following, we discuss the modification of these profiles for the 1LM constituent, which shows dependence on both d_{BP} and λ_{ex}.

RESULTS AND DISCUSSION

Figure 1a shows an optical microscopy image of a 59 nm-BP/1LM vdWH, with the BP flake stacked on top of the 1LM flake. Isolated BP and 1LM flakes are visible adjacent to the BP/1LM. Figure 1b presents the Raman spectra of the individual flakes and their heterostructure at λ_{ex} = 532 nm. All characteristic phonon modes are identified: BP's A_g^1, B_{2g}, and A_g^2, along with 1LM's A_1' and E' modes. The heterostructure spectrum essentially reproduces the superposition of its constituent spectra.

https://doi.org/10.1021/acsaom.5c00385
ACS Appl. Opt. Mater. 2025, 3, 2655−2661

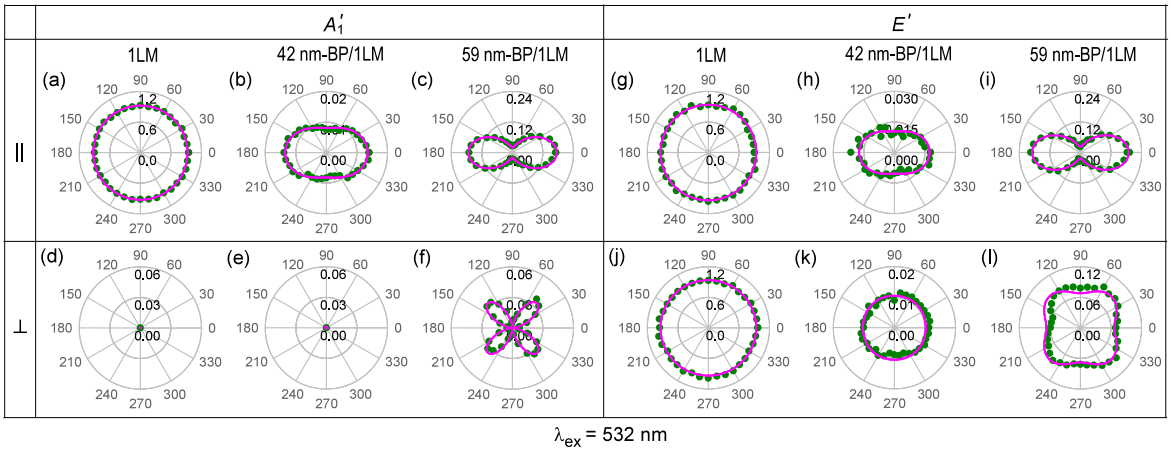

Figure 3. ARPR intensity profiles of the (a–f) A_1' and (g–l) E' modes of 1LM and the 1LM constituent in BP/1LM with d_{BP} of 42 and 59 nm, measured under both (a–c, g–i) parallel and (d–f, j–l) cross-polarization configurations at λ_{ex} of 532 nm.

ARPR measurements were conducted on both the BP/1LM and standalone 1LM under parallel and cross-polarization configurations, with the experimental setup illustrated in Figure 1c. Although 1LM is inserted between BP and the SiO_2/Si substrate, the intensities $I(A_g^1)$ and $I(A_g^2)$ of the BP constituent follow the previously reported ARPR intensity profile of a standalone BP flake[8] with similar thickness in both parallel and cross-polarization configurations at 532 nm due to the small thickness of 1LM.

For standalone 1LM, $I(A_1')$ and $I(E')$ remain constant from $\theta = 0°$ to 360° under parallel polarization (Figure 1d). Under cross-polarization (Figure 1e) only the E' mode appears, and the A_1' mode vanishes. These observations align with the Raman selection rules for 1LM, confirming its in-plane isotropy. In contrast, the 1LM constituent in BP/1LM exhibits a strong angular dependence in the parallel polarization configuration (Figure 1f), where $I(A_1')$ and $I(E')$ modulate with a 180° periodicity. Under cross-polarization (Figure 1g), both A_1' and E' modes appear, with $I(A_1')$ displaying 90° periodicity. This behavior deviates sharply from the isotropic response of standalone 1LM but matches BP's symmetry, indicating that the optical anisotropy of BP modifies the Raman response of 1LM in the heterostructure.

When incident light passes through the BP layer to excite Raman signals in the 1LM constituent and the Raman-scattered light subsequently passes back through the BP layer to reach the CCD, the birefringence and linear dichroism of BP alter the polarization states of both the incident and scattered light. This polarization modulation depends on the angle between the initial polarization direction of the incident light and the ZZ (or AC) axis of BP. Consequently, the initially isotropic $I(A_1', \parallel, \theta)$ of the 1LM constituent should resemble the ARPR intensity profile of the A_g^1 and A_g^2 modes in BP. Indeed, the angular dependence of $I(A_1')$ closely follows that of the A_g^1 mode in the BP constituent due to its small ϕ_{ca}^{int} (~16.9°) in BP at 532 nm.[8] However, it differs significantly from the nearly circular profile of the A_g^2 mode. This distinction arises primarily from the large ϕ_{ca}^{int} (~ −78.1°) and $|c^{int}|/|a^{int}|$ (~2.01) of the A_g^2 mode at 532 nm. The birefringence and linear dichroism of BP further enable the observation of 1LM's otherwise forbidden A_1' mode in cross-polarization configurations, exhibiting an angular dependence profile remarkably similar to that of BP's A_g^1 mode. 1LM's $I(E', \parallel, \theta)$ closely resembles BP's $I(A_g^1, \parallel, \theta)$ profile, while $I(E', \perp, \theta)$ displays a markedly different ARPR pattern from the $I(A_g^1, \perp, \theta)$ of BP owing to E' mode's doubly degenerate nature and dual Raman tensor characteristics.

To quantitatively model the angular dependence of $I(A_1')$ and $I(E')$ for the 1LM constituent, in addition to the birefringence/linear dichroism of the BP constituent, the interference effects (Figure 2a) in the air/BP/1LM/substrate multilayer system must be further considered. The derived angular dependencies for parallel and cross-polarization configurations are given by eqs 6–9. Figure 2b depicts the corresponding calculated d_{BP}-dependent $I_{ZZ}(A_1', \parallel)$ and $I_{AC}(A_1', \parallel)$ for λ_{ex} = 532 nm. With increasing d_{BP}, $I_{ZZ}(A_1', \parallel)$ and $I_{AC}(A_1', \parallel)$ show periodic fluctuations with an overall downward trend. The periodic fluctuations provide evidence that the interference effects in the air/BP/1LM/substrate system is very important for understanding the ARPR intensity of ALMs.[8] The ratio $I_{ZZ}(A_1', \parallel)/I_{AC}(A_1', \parallel)$ displays periodic fluctuations but with an overall upward trend (Figure 2c). This upward trend behavior stems from the linear dichroism effect, i.e., stronger absorption along AC ($\kappa_{AC} > \kappa_{ZZ}$) in the visible regime. It becomes more pronounced with larger d_{BP}, leading to progressively enhanced anisotropic influence of BP on $I_{ZZ}(A_1', \parallel)/I_{AC}(A_1', \parallel)$ of the 1LM constituent, as evidenced in Figure 2c. The d_{BP} dependence of $I_{ZZ(AC)}(E', \parallel)$ and $I_{ZZ(AC)}(E', \perp)$ is depicted in Figures S1 and S2.

Next, we investigate experimental d_{BP}-dependent ARPR intensity profiles of the 1LM constituent excited by λ_{ex} = 532 nm, as depicted in Figure 3a–l for 42 nm-BP/1LM and 59 nm-BP/1LM along with 1LM. The calculated ARPR intensity profiles (solid lines) of $I(A_1', \parallel, \theta)$, $I(A_1', \perp, \theta)$, $I(E', \parallel, \theta)$ and $I(E', \perp, \theta)$ fit the experimental ones (solid circles) well. Although 59 nm BP shows stronger absorption than 42 nm BP, $I(A_1', \parallel, \theta)$ and $I(E', \parallel, \theta)$ of the 1LM constituent in 59 nm-BP/1LM is much stronger than that in 42 nm-BP/1LM under the parallel polarization configuration. The experimental results for the A_1' mode of the 1LM constituent (open circles and squares for 59 nm-BP/1LM and 42 nm-BP/1LM, respectively) agree with the calculations in Figure 2b, consistent with the cases of the E' mode in Figure S2a,c. This is attributed to interference effects in the air/BP/1LM/substrate system.

For the 1LM constituent in BP/1LM, the initially isotropic $I(A_1', \parallel, \theta)$ and $I(E', \parallel, \theta)$ exhibit a two-lobed shape due to the optical anisotropy of the BP constituent. As d_{BP} increases, the

https://doi.org/10.1021/acsaom.5c00385
ACS Appl. Opt. Mater. 2025, 3, 2655−2661

condition $|F^{AC}_{i(s)}| \ll |F^{ZZ}_{i(s)}|$ causes $I(A_1', \parallel, \theta)$ and $I(E', \parallel, \theta)$ to follow $\cos^4\theta$ dependencies described by eqs 6 and 7, resulting in two-lobed polar plots with vanishing intensity along the AC direction. However, $I(A_1', \perp, \theta)$ exhibits a butterfly shaped pattern due to the birefringence and linear dichroism of the BP constituent, which modifies the polarization vector and amplitude of the incident light before it reaches the 1LM layer. This causes $I(A_1', \perp, \theta)$ to be observable and follow a butterfly shaped $\sin^2 2\theta$ dependence. Similarly, initially isotropic $I(E', \perp, \theta)$ transforms into a rounded-square shape.

The birefringence and linear dichroism of ALMs, along with interference effects in ALM-based multilayer systems, exhibit strong sensitivity to λ_{ex}, indicating that the optical anisotropy of BP significantly influences the ARPR intensity of the 1LM constituent in a wavelength-dependent manner. Figure 4a,b

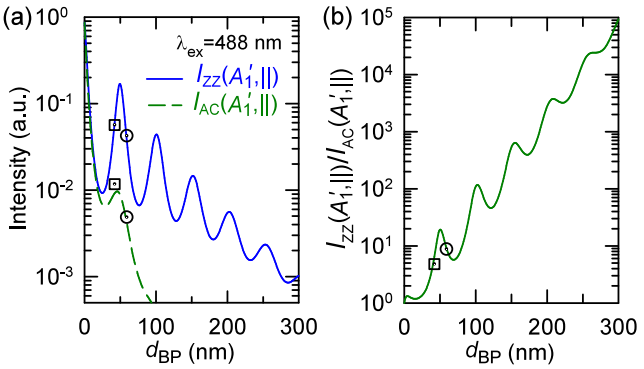

Figure 4. (a) $I_{ZZ}(A_1', \parallel)$, $I_{AC}(A_1', \parallel)$, and (b) $I_{ZZ}(A_1', \parallel)/I_{AC}(A_1', \parallel)$ of the 1LM constituent in BP/1LM vdWHs deposited on 90 nm-SiO_2/Si substrate as a function of d_{BP}, λ_{ex} = 488 nm. Open circles and squares denote normalized Raman intensities of the 1LM component in 59 nm-BP/1LM and 42 nm-BP/1LM heterostructures, respectively.

presents calculated d_{BP}-dependent $I_{ZZ}(A_1', \parallel)$, $I_{AC}(A_1', \parallel)$, and their ratio $I_{ZZ}(A_1', \parallel)/I_{AC}(A_1', \parallel)$ for λ_{ex} = 488 nm, revealing patterns similar to those in Figure 2b,c but with steeper overall downward (Figure 4a) and upward (Figure 4b) trends due to BP's stronger absorption at shorter wavelengths. Notably, $I_{AC}(A_1', \parallel)$ at 488 nm demonstrates a sharper decline compared to that at 532 nm excitation, reflecting the enhanced linear dichroism of BP at the shorter wavelength. Additionally, the fluctuation periodicity of both $I_{ZZ}(A_1', \parallel)$ and $I_{AC}(A_1', \parallel)$ differs from the 532 nm case, resulting in stronger intensities at d_{BP} = 42 nm than at 59 nm, exhibiting a reversal of the trend observed for λ_{ex} = 532 nm. The experimental results for d_{BP} = 42 and 59 nm, denoted by open squares and circles in Figure 4a,b, confirm the theoretical predictions.

As shown in Figure 5a–l, ARPR measurements at λ_{ex} = 488 nm reproduce the calculated intensity profiles well. The initially isotropic $I(A_1', \parallel, \theta)$ and $I(E', \parallel, \theta)$ of 1LM in the BP/1LM system exhibit a distinct two-lobed shape, while $I(E', \perp, \theta)$ transforms into a rounded-square profile. Both the experimental $I(A_1', \parallel, \theta)$ and $I(E', \parallel, \theta)$ intensities (blue scatters) demonstrate stronger signals in the 42 nm-BP/1LM system compared with the 59 nm-BP/1LM system, consistent with the computational predictions (pink lines).

CONCLUSIONS

This study demonstrates that the originally isotropic Raman signals of monolayer MoS_2 acquire pronounced angular dependence when integrated with anisotropic BP flakes, an emergent anisotropy originating from the combined effects of BP's in-plane optical anisotropy (birefringence and linear dichroism) and multilayer interference in the BP/1LM/substrate structure. These factors induce significant alterations in the polarization vector and amplitude of both the incident light reaching the 1LM constituent and the Raman-scattered light emanating from it. The calculated results show excellent agreement with the measured ARPR intensity profiles of the 1LM constituent for different d_{BP} values and λ_{ex}. This paves the way for a comprehensive understanding of ARPR responses from both isotropic and anisotropic constituents and enabling tailored manipulation of the optical response of isotropic components within ALM-based vdWHs.

ASSOCIATED CONTENT

Supporting Information

The Supporting Information is available free of charge at https://pubs.acs.org/doi/10.1021/acsaom.5c00385.

Calculations of the enhancement factors by the transfer matrix method, complex refractive indices used in the

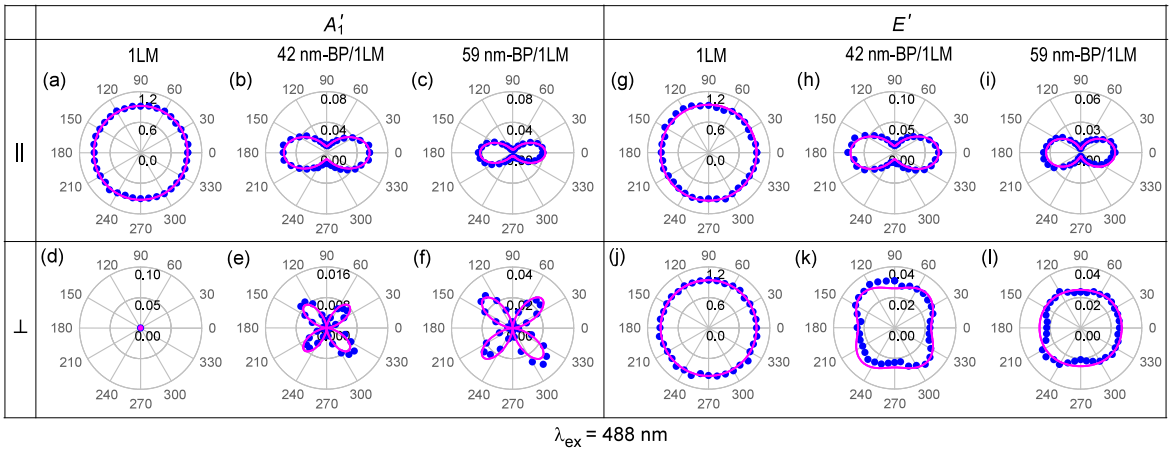

Figure 5. ARPR intensity profiles of the (a–f) A_1' and (g–l) E' modes of 1LM and the 1LM constituent in BP/1LM with d_{BP} of 42 and 59 nm, measured under both (a–c, g–i) parallel and (d–f, j–l) cross-polarization configurations at λ_{ex} of 488 nm.

https://doi.org/10.1021/acsaom.5c00385
ACS Appl. Opt. Mater. 2025, 3, 2655–2661

calculations, and d_{BP} dependence of $I_{ZZ(AC)}(E', \parallel)$ and $I_{ZZ(AC)}(E', \perp)$ (PDF)

AUTHOR INFORMATION

Corresponding Author

Ping-Heng Tan − *State Key Laboratory of Semiconductor Physics and Chip Technologies, Institute of Semiconductors, Chinese Academy of Sciences, Beijing 100083, China; Center of Materials Science and Optoelectronics Engineering, University of Chinese Academy of Sciences, Beijing 100049, China;* orcid.org/0000-0001-6575-1516; Email: phtan@semi.ac.cn

Authors

Zi-Han Zhang − *State Key Laboratory of Semiconductor Physics and Chip Technologies, Institute of Semiconductors, Chinese Academy of Sciences, Beijing 100083, China; Center of Materials Science and Optoelectronics Engineering, University of Chinese Academy of Sciences, Beijing 100049, China*

Chen-Kai Liu − *State Key Laboratory of Semiconductor Physics and Chip Technologies, Institute of Semiconductors, Chinese Academy of Sciences, Beijing 100083, China; Center of Materials Science and Optoelectronics Engineering, University of Chinese Academy of Sciences, Beijing 100049, China*

Jia-Liang Xie − *State Key Laboratory of Semiconductor Physics and Chip Technologies, Institute of Semiconductors, Chinese Academy of Sciences, Beijing 100083, China; Center of Materials Science and Optoelectronics Engineering, University of Chinese Academy of Sciences, Beijing 100049, China*

Rui Mei − *State Key Laboratory of Semiconductor Physics and Chip Technologies, Institute of Semiconductors, Chinese Academy of Sciences, Beijing 100083, China; Center of Materials Science and Optoelectronics Engineering, University of Chinese Academy of Sciences, Beijing 100049, China;* orcid.org/0009-0005-5684-5306

Tao Liu − *State Key Laboratory of Semiconductor Physics and Chip Technologies, Institute of Semiconductors, Chinese Academy of Sciences, Beijing 100083, China; Center of Materials Science and Optoelectronics Engineering, University of Chinese Academy of Sciences, Beijing 100049, China*

Miao-Ling Lin − *State Key Laboratory of Semiconductor Physics and Chip Technologies, Institute of Semiconductors, Chinese Academy of Sciences, Beijing 100083, China; Center of Materials Science and Optoelectronics Engineering, University of Chinese Academy of Sciences, Beijing 100049, China;* orcid.org/0000-0001-5838-8237

Complete contact information is available at: https://pubs.acs.org/10.1021/acsaom.5c00385

Author Contributions

[▽]Z.-H.Z. and C.-K.L. contributed equally to this work.

Notes

The authors declare no competing financial interest.

ACKNOWLEDGMENTS

The authors acknowledge the support from the National Key Research and Development Program of China (Grant No. 2023YFA1407000), the Strategic Priority Research Program of CAS (Grant No. XDB0460000), National Natural Science Foundation of China (Grant Nos. 12322401, 12127807, and 12393832), Beijing Nova Program (Grant No. 20230484301), Youth Innovation Promotion Association, Chinese Academy of Sciences (No. 2023125), and CAS Project for Young Scientists in Basic Research (YSBR-026).

REFERENCES

(1) Liu, H.; Du, Y.; Deng, Y.; Ye, P. D. Semiconducting black phosphorus: synthesis, transport properties and electronic applications. *Chem. Soc. Rev.* **2015**, *44*, 2732−2743.

(2) Carvalho, A.; Wang, M.; Zhu, X.; Rodin, A. S.; Su, H.; Castro Neto, A. H. Phosphorene: from theory to applications. *Nat. Rev. Mater.* **2016**, *1*, 16061.

(3) Xia, F.; Wang, H.; Hwang, J. C. M.; Neto, A. H. C.; Yang, L. Black phosphorus and its isoelectronic materials. *Nat. Rev. Phys.* **2019**, *1*, 306−317.

(4) Yuan, H.; et al. Polarization-sensitive broadband photodetector using a black phosphorus vertical p−n junction. *Nat. Nanotechnol.* **2015**, *10*, 707−713.

(5) Li, L.; Yu, Y.; Ye, G. J.; Ge, Q.; Ou, X.; Wu, H.; Feng, D.; Chen, X. H.; Zhang, Y. Black phosphorus field-effect transistors. *Nat. Nanotechnol.* **2014**, *9*, 372−377.

(6) Fei, R.; Faghaninia, A.; Soklaski, R.; Yan, J.-A.; Lo, C.; Yang, L. Enhanced Thermoelectric Efficiency via Orthogonal Electrical and Thermal Conductances in Phosphorene. *Nano Lett.* **2014**, *14*, 6393−6399.

(7) Ribeiro, H. B.; Pimenta, M. A.; de Matos, C. J. S.; Moreira, R. L.; Rodin, A. S.; Zapata, J. D.; de Souza, E. A. T.; Castro Neto, A. H. Unusual Angular Dependence of the Raman Response in Black Phosphorus. *ACS Nano* **2015**, *9*, 4270−4276.

(8) Xie, J.-L.; Liu, T.; Leng, Y.-C.; Mei, R.; Wu, H.; Liu, C.-K.; Wang, J.-H.; Li, Y.; Yu, X.-F.; Lin, M.-L.; Tan, P.-H. Quantitatively Predicting Angle-Resolved Polarized Raman Intensity of Anisotropic Layered Materials. *Adv. Mater.* **2025**, *37*, 2506241.

(9) Kim, J.; Lee, J.-U.; Lee, J.; Park, H. J.; Lee, Z.; Lee, C.; Cheong, H. Anomalous polarization dependence of Raman scattering and crystallographic orientation of black phosphorus. *Nanoscale* **2015**, *7*, 18708−18715.

(10) Phaneuf-L'Heureux, A.-L.; Favron, A.; Germain, J.-F.; Lavoie, P.; Desjardins, P.; Leonelli, R.; Martel, R.; Francoeur, S. Polarization-Resolved Raman Study of Bulk-like and Davydov-Induced Vibrational Modes of Exfoliated Black Phosphorus. *Nano Lett.* **2016**, *16*, 7761−7767.

(11) Mao, N.; Wu, J.; Han, B.; Lin, J.; Tong, L.; Zhang, J. Birefringence-Directed Raman Selection Rules in 2D Black Phosphorus Crystals. *Small* **2016**, *12*, 2627−2633.

(12) Lin, M.-L.; Leng, Y.-C.; Cong, X.; Meng, D.; Wang, J.; Li, X.-L.; Yu, B.; Liu, X.-L.; Yu, X.-F.; Tan, P.-H. Understanding angle-resolved polarized Raman scattering from black phosphorus at normal and oblique laser incidences. *Sci. Bull.* **2020**, *65*, 1894−1900.

(13) Wen, T.; Zhang, M.; Li, J.; Jiao, C.; Pei, S.; Wang, Z.; Xia, J. Orientation-polarization dependence of pressure-induced Raman anomalies in anisotropic 2D ReS_2. *Nanoscale Horiz.* **2023**, *8*, 516−521.

(14) Ling, X.; et al. Anisotropic Electron-Photon and Electron-Phonon Interactions in Black Phosphorus. *Nano Lett.* **2016**, *16*, 2260−2267.

(15) Mao, N.; Wang, X.; Lin, Y.; Sumpter, B. G.; Ji, Q.; Palacios, T.; Huang, S.; Meunier, V.; Dresselhaus, M. S.; Tisdale, W. A.; Liang, L.; Ling, X.; Kong, J. Direct Observation of Symmetry-Dependent Electron-Phonon Coupling in Black Phosphorus. *J. Am. Chem. Soc.* **2019**, *141*, 18994−19001.

(16) Zou, B.; Wei, Y.; Zhou, Y.; Ke, D.; Zhang, X.; Zhang, M.; Yip, C.-T.; Chen, X.; Li, W.; Sun, H. Unambiguous determination of crystal orientation in black phosphorus by angle-resolved polarized Raman spectroscopy. *Nanoscale Horiz.* **2021**, *6*, 809−818.

(17) Ribeiro, H. B.; Villegas, C. E. P.; Bahamon, D. A.; Muraca, D.; Castro Neto, A. H.; de Souza, E. A. T.; Rocha, A. R.; Pimenta, M. A.; de Matos, C. J. S. Edge phonons in black phosphorus. *Nat. Commun.* **2016**, *7*, 12191.
(18) Guo, Y.; Zhang, W.; Wu, H.; Han, J.; Zhang, Y.; Lin, S.; Liu, C.; Xu, K.; Qiao, J.; Ji, W.; Chen, Q.; Gao, S.; Zhang, W.; Zhang, X.; Chai, Y. Discovering the forbidden Raman modes at the edges of layered materials. *Sci. Adv.* **2018**, *4*, eaau6252.
(19) Loudon, R. The Raman effect in crystals. *Adv. Phys.* **1964**, *13*, 423−482.
(20) Zong, X.; Hu, H.; Ouyang, G.; Wang, J.; Shi, R.; Zhang, L.; Zeng, Q.; Zhu, C.; Chen, S.; Cheng, C.; Wang, B.; Zhang, H.; Liu, Z.; Huang, W.; Wang, T.; Wang, L.; Chen, X. Black phosphorus-based van der Waals heterostructures for mid-infrared light-emission applications. *Light Sci. Appl.* **2020**, *9*, 114.
(21) Zheng, B.; Wang, J.; Wang, Q.; Su, X.; Huang, T.; Li, S.; Wang, F.; Shi, Y.; Wang, X. Quantum criticality of excitonic Mott metal-insulator transitions in black phosphorus. *Nat. Commun.* **2022**, *13*, 7797.
(22) Deng, Y.; Luo, Z.; Conrad, N. J.; Liu, H.; Gong, Y.; Najmaei, S.; Ajayan, P. M.; Lou, J.; Xu, X.; Ye, P. D. Black phosphorus-monolayer MoS_2 van der Waals heterojunction p−n Diode. *ACS Nano* **2014**, *8*, 8292−8299.
(23) Bullock, J.; Amani, M.; Cho, J.; Chen, Y.-Z.; Ahn, G. H.; Adinolfi, V.; Shrestha, V. R.; Gao, Y.; Crozier, K. B.; Chueh, Y.-L.; Javey, A. Polarization-resolved black phosphorus/molybdenum disulfide mid-wave infrared photodiodes with high detectivity at room temperature. *Nat. Photonics* **2018**, *12*, 601−607.
(24) Wu, P.; Ye, L.; Tong, L.; Wang, P.; Wang, Y.; Wang, H.; Ge, H.; Wang, Z.; Gu, Y.; Zhang, K.; Yu, Y.; Peng, M.; Wang, F.; Huang, M.; Zhou, P.; Hu, W. Van der Waals two-color infrared photodetector. *Light Sci. Appl.* **2022**, *11*, 6.
(25) Jawa, H.; Varghese, A.; Ghosh, S.; Sahoo, S.; Yin, Y.; Medhekar, N. V.; Lodha, S. Wavelength-Controlled Photocurrent Polarity Switching in BP-MoS_2 Heterostructure. *Adv. Funct. Mater.* **2022**, *32*, 2112696.
(26) Li, D.; Wang, B.; Chen, M.; Zhou, J.; Zhang, Z. Gate-Controlled BP−WSe_2 Heterojunction Diode for Logic Rectifiers and Logic Optoelectronics. *Small* **2017**, *13*, 1603726.
(27) Ye, L.; Wang, P.; Luo, W.; Gong, F.; Liao, L.; Liu, T.; Tong, L.; Zang, J.; Xu, J.; Hu, W. Highly polarization sensitive infrared photodetector based on black phosphorus-on-WSe_2 photogate vertical heterostructure. *Nano Energy* **2017**, *37*, 53−60.
(28) Mao, N.; Zhang, S.; Wu, J.; Tian, H.; Wu, J.; Xu, H.; Peng, H.; Tong, L.; Zhang, J. Investigation of black phosphorus as a nano-optical polarization element by polarized Raman spectroscopy. *Nano Res.* **2018**, *11*, 3154−3163.
(29) Castellanos-Gomez, A.; Buscema, M.; Molenaar, R.; Singh, V.; Janssen, L.; van der Zant, H. S. J.; Steele, G. A. Deterministic transfer of two-dimensional materials by all-dry viscoelastic stamping. *2D Mater.* **2014**, *1*, No. 011002.
(30) Zhang, X.; Qiao, X.-F.; Shi, W.; Wu, J.-B.; Jiang, D.-S.; Tan, P.-H. Phonon and Raman scattering of two-dimensional transition metal dichalcogenides from monolayer, multilayer to bulk material. *Chem. Soc. Rev.* **2015**, *44*, 2757−2785.
(31) Liu, T.; Xie, J.-L.; Mei, R.; Lin, M.-L.; Tan, P.-H. Asymmetrical Angle-resolved Polarized Raman Intensity Profiles Measured by Commercial Half-wave Plates with Inevitable Retardance Error. *J. Phys. Chem. C* **2024**, *128*, 21001−21008.
(32) Ermolaev, G. A.; Stebunov, Y. V.; Vyshnevyy, A. A.; Tatarkin, D. E.; Yakubovsky, D. I.; Novikov, S. M.; Baranov, D. G.; Shegai, T.; Nikitin, A. Y.; Arsenin, A. V.; Volkov, V. S. Broadband optical properties of monolayer and bulk MoS2. *npj 2D Mater. Appl.* **2020**, *4*, 21.
(33) *Handbook of Optical Constants of Solids*; Palik, E. D., Ed.; Academic Press, San Diego, 1998.

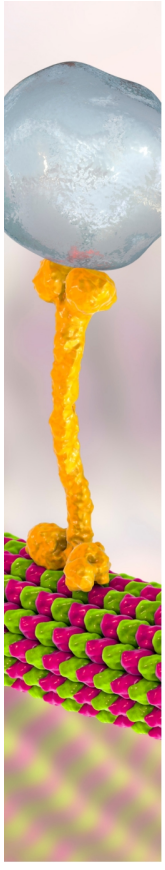

https://doi.org/10.1021/acsaom.5c00385
ACS Appl. Opt. Mater. 2025, 3, 2655−2661

Supporting Information

Anisotropic Raman Response from Isotropic Constituents in BP/MoS_2 Heterostructures

Zi-Han Zhang,[†,‡,¶] Chen-Kai Liu,[†,‡,¶] Jia-Liang Xie,[†,‡] Rui Mei,[†,‡] Tao Liu,[†,‡] Miao-Ling Lin,[†,‡] and Ping-Heng Tan[*,†,‡]

†*State Key Laboratory of Semiconductor Physics and Chip Technologies, Institute of Semiconductors, Chinese Academy of Sciences, Beijing 100083, China*

‡*Center of Materials Science and Optoelectronics Engineering, University of Chinese Academy of Sciences, Beijing 100049, China*

¶*These authors contributed equally to this work.*

E-mail: phtan@semi.ac.cn

Computational Methods

BP/1LM vdWH on SiO_2/Si substrate form a five-layer dielectric structure air/BP/1LM/SiO_2/Si with complex refractive indexes $\tilde{n}_0/\tilde{n}_1/\tilde{n}_2/\tilde{n}_3/\tilde{n}_4$, as shown in Figure 2a, where d_μ (d_1=d_{BP}, d_2=d_{1LM} and d_3=$d_{\mathrm{SiO_2}}$) and $\tilde{n}_\mu$ are the thickness and complex refractive index of the medium μ. $\tilde{n}_1$ is set to be $\tilde{n}_{\mathrm{ZZ}}$ and $\tilde{n}_{\mathrm{AC}}$, respectively, to calculate $F^{\mathrm{ZZ}}_{\mathrm{i(s)}}(z)$ and $F^{\mathrm{AC}}_{\mathrm{i(s)}}(z)$. The calculation process using the transfer matrix method[1,2] is as follows: According to Fresnel's equations, the transfer matrix at the interface between the medium μ and medium ν is denoted as $\mathrm{A}_{\mu\nu}$. The propagation within the medium ν is described by the propagation matrix B_ν. $\mathrm{A}_{\mu\nu}$ and

B_ν are given by:

$$\mathrm{A}_{\mu\nu} = \frac{1}{t_{\mu\nu}} \begin{pmatrix} 1 & r_{\mu\nu} \\ r_{\mu\nu} & 1 \end{pmatrix}, \ \mathrm{B}_\nu(z_\nu) = \begin{pmatrix} e^{-\mathrm{i}\delta_\nu(z_\nu)} & 0 \\ 0 & e^{\mathrm{i}\delta_\nu(z_\nu)} \end{pmatrix} \tag{S1}$$

where $t_{\mu\nu} = \frac{2\tilde{n}_\mu}{\tilde{n}_\mu + \tilde{n}_\nu}$ and $r_{\mu\nu} = \frac{\tilde{n}_\mu - \tilde{n}_\nu}{\tilde{n}_\mu + \tilde{n}_\nu}$ are the transmission and reflection coefficients between the medium μ and medium ν, and $\delta_\nu(z_\nu) = 2\pi\tilde{n}_\nu z_\nu/\lambda$ is the phase factor within the medium ν.

First, we calculate the electric field components of the incident light by considering its propagation within the structure. Based on Equation S1, the relationship between the electric field components of the incident laser at the air/BP interface (on the air side) and those at depth z in the 1LM constituent is expressed by the following equation:

$$\begin{pmatrix} E_{\mathrm{i}0}^+ \\ E_{\mathrm{i}0}^- \end{pmatrix} = \mathrm{A}_{01}\mathrm{B}_1(d_1)\mathrm{A}_{12}\mathrm{B}_2(z) \begin{pmatrix} E_{\mathrm{i}2}^+(z) \\ E_{\mathrm{i}2}^-(z) \end{pmatrix} \tag{S2}$$

where + and - denote the downward and upward propagating directions, respectively. $E_{\mathrm{i}0}^+$ represents the downward-propagating incident electric field component, and $E_{\mathrm{i}0}^-$ is the upward-propagating incident electric field component. $E_{\mathrm{i}2}^+(z)$ and $E_{\mathrm{i}2}^-(z)$ correspond to the electric field components of the excitation laser propagating downward and upward to depth z within the 1LM constituent. The boundary condition for the Si substrate is considered to get the following equation:

$$\begin{pmatrix} E_{\mathrm{i}0}^+ \\ E_{\mathrm{i}0}^- \end{pmatrix} = \mathrm{A}_{01}\mathrm{B}_1(d_1)\mathrm{A}_{12}\mathrm{B}_2(d_1)\mathrm{A}_{23}\mathrm{B}_3(d_3)\mathrm{A}_{34} \begin{pmatrix} E_{\mathrm{i}4}^+(0) \\ 0 \end{pmatrix} \tag{S3}$$

where $E_{\mathrm{i}4}^+(0)$ is the electric field components at the SiO_2/Si interface (on the Si side). From Eq. (S3), the relationship between the incident electric field component at the air/BP inter-

face and that at the SiO_2/Si interface is obtained:

$$E_{\mathrm{i0}}^{+} = \mathrm{M}_{11} E_{\mathrm{i4}}^{+}(0) \tag{S4}$$

where $\mathrm{M} = \mathrm{A}_{01}\mathrm{B}_1(d_1)\mathrm{A}_{12}\mathrm{B}_2(d_2)\mathrm{A}_{23}\mathrm{B}_3(d_3)\mathrm{A}_{34}$. By combining Equation S2 and S3, we obtain:

$$\begin{pmatrix} E_{\mathrm{i2}}^{+}(z) \\ E_{\mathrm{i2}}^{-}(z) \end{pmatrix} = \mathrm{N} \begin{pmatrix} E_{\mathrm{i4}}^{+}(0) \\ 0 \end{pmatrix} \tag{S5}$$

where $\mathrm{N} = \mathrm{B}_2(d_2 - z)\mathrm{A}_{23}\mathrm{B}_3(d_3)\mathrm{A}_{34}$. By combining Equation S4 and S5, $E_{\mathrm{i2}}^{+}(z)$ and $E_{\mathrm{i2}}^{-}(z)$ are derived:

$$E_{\mathrm{i2}}^{+}(z) = \mathrm{N}_{11} E_{\mathrm{i4}}^{+}(0),\ E_{\mathrm{i2}}^{-}(z) = \mathrm{N}_{21} E_{\mathrm{i4}}^{+}(0) \tag{S6}$$

The total electric field of the excitation light at depth z in the 1LM constituent, $E_{\mathrm{i2}}(z)$, is the superposition of $E_{\mathrm{i2}}^{+}(z)$ and $E_{\mathrm{i2}}^{-}(z)$.

Next, we calculate the electric field components of the Raman-scattered light. As the Raman scattering occurs in all directions, both upward (U) and downward (D) propagation paths must be considered. For the upward propagating scattered light, the relationship between the electric field components at the air/BP interface (on the air side) and those at the scattering site, located at depth z in the 1LM constituent is given by:

$$\begin{pmatrix} 0 \\ E_{\mathrm{sU0}}^{-} \end{pmatrix} = \mathrm{A}_{01}\mathrm{B}_1(d_1)\mathrm{A}_{12} \left[\mathrm{B}_2(d_2) \begin{pmatrix} E_{\mathrm{sU2}}^{+}(d_2) \\ E_{\mathrm{sU2}}^{-}(d_2) \end{pmatrix} + \mathrm{B}_2(z) \begin{pmatrix} 0 \\ E_{\mathrm{sU2}}^{-}(z) \end{pmatrix} \right] \tag{S7}$$

E_{sU0}^{-} is the electric field component of the Raman-scattered light propagating along the U path at the air/BP interface (on the air side). $E_{\mathrm{sU2}}^{+}(d_2)$ and $E_{\mathrm{sU2}}^{-}(d_2)$ are the electric field components of the Raman-scattered light propagating along the U path at the 1LM side of the 1LM/SiO_2 interface, while $E_{\mathrm{sU2}}^{-}(z)$ denotes the electric field component of the Raman-scattered light propagating along the U path at the scattering site in the 1LM constituent.

Similarly, for the downward propagating Raman-scattered light, the transfer equation is expressed as follows:

$$\begin{pmatrix} 0 \\ E^{-}_{\mathrm{sD0}} \end{pmatrix} = \mathrm{A}_{01}\mathrm{B}_1(d_1)\mathrm{A}_{12}\left[\mathrm{B}_2(d_2)\begin{pmatrix} E^{+}_{\mathrm{sD2}}(d_2) \\ E^{-}_{\mathrm{sD2}}(d_2) \end{pmatrix} - \mathrm{B}_2(z)\begin{pmatrix} E^{+}_{\mathrm{sD2}}(z) \\ 0 \end{pmatrix}\right] \tag{S8}$$

E^{-}_{sD0} is the electric field component of the scattered light propagating along the D path at the air/BP interface (on the air side). $E^{+}_{\mathrm{sD2}}(d_2)$ and $E^{-}_{\mathrm{sD2}}(d_2)$ are the electric field components of the scattered light propagating along the D path at the 1LM side of the 1LM/SiO_2 interface, while $E^{+}_{\mathrm{sD2}}(z)$ denotes the electric field component of the Raman-scattered light propagating along the D path at the scattering site in the 1LM constituent. After considering the boundary condition of the Si substrate, the transfer equation can be expressed as:

$$\begin{pmatrix} E^{+}_{\mathrm{sU(D)2}}(d_2) \\ E^{-}_{\mathrm{sU(D)2}}(d_2) \end{pmatrix} = \mathrm{A}_{23}\mathrm{B}_3(d_3)\mathrm{A}_{34}\begin{pmatrix} E^{+}_{\mathrm{sU(D)4}}(0) \\ 0 \end{pmatrix} \tag{S9}$$

Similar to the case of the incident laser, by combining the Equation S7-S9, we have:

$$E^{+}_{\mathrm{sU4}}(0) = -\frac{\mathrm{P}_{12}}{\mathrm{M}_{11}}E^{-}_{\mathrm{sU2}}(z),\ E^{+}_{\mathrm{sD4}}(0) = \frac{\mathrm{P}_{11}}{\mathrm{M}_{11}}E^{+}_{\mathrm{sD2}}(z) \tag{S10}$$

where $\mathrm{P} = \mathrm{A}_{01}\mathrm{B}_1(d_1)\mathrm{A}_{12}\mathrm{B}_2(z)$ represents the 2×2 transfer matrix that relates the electric field components of the scattered light at the scattering site to those at the Si side of the SiO_2/Si interface, and P_{11} and P_{12} are the two elements of P. From the Equation S7-S10, the electric field components of the scattered light propagating along both the U and D paths at the air/BP interface (on the air side) are determined:

$$E^{-}_{\mathrm{sU0}} = \left(\mathrm{P}_{22} - \frac{\mathrm{M}_{21}\mathrm{P}_{12}}{\mathrm{M}_{11}}\right)E^{-}_{\mathrm{sU2}}(z),\ E^{-}_{\mathrm{sD0}} = \left(\frac{\mathrm{M}_{21}\mathrm{P}_{11}}{\mathrm{M}_{11}} - \mathrm{P}_{21}\right)E^{+}_{\mathrm{sD2}}(z) \tag{S11}$$

The total electric field of the Raman-scattered light emitted from depth z in the 1LM con-

stituent, $E_{\mathrm{s}}(z)$, is the superposition of $E^{-}_{\mathrm{sU2}}(z)$ and $E^{+}_{\mathrm{sD2}}(z)$. Provided that the Raman scattering is isotropic, $E^{-}_{\mathrm{sU2}}(z)$ equals to $E^{+}_{\mathrm{sD2}}(z)$.

The interference factor $F_{\mathrm{i(s)}}(z)$ for the electric field components of incident (or Raman-scattered) light at depth z can be obtained:

$$F_{\mathrm{i}}(z) = \frac{E_{\mathrm{i2}}(z)}{E^{+}_{\mathrm{i0}}},\ F_{\mathrm{s}}(z) = \frac{E^{-}_{\mathrm{sU0}}}{E^{-}_{\mathrm{sU2}}(z)} + \frac{E^{-}_{\mathrm{sD0}}}{E^{+}_{\mathrm{sD2}}(z)} \tag{S12}$$

By setting $\tilde{n}_1$ to be $\tilde{n}_{\mathrm{ZZ}}$ and $\tilde{n}_{\mathrm{AC}}$ respectively, $F^{\mathrm{ZZ}}_{\mathrm{i(s)}}(z)$ and $F^{\mathrm{AC}}_{\mathrm{i(s)}}(z)$ can be obtained. The complex refractive indices used in the calculations are summarized in Table S1.

Table S1: Complex refractive indices of BP, 1LM, SiO_2, and Si at λ_{ex} =532 nm and 488 nm.

Material	$\tilde{n}$@532nm	$\tilde{n}$@488 nm
BP(ZZ)[2]	$4.48 + 0.13\mathrm{i}$	$4.79 + 0.27\mathrm{i}$
BP(AC)[2]	$4.39 + 0.54\mathrm{i}$	$4.50 + 1.02\mathrm{i}$
1LM[3]	$4.37 + 1.25\mathrm{i}$	$4.97 + 1.25\mathrm{i}$
SiO_2[4]	1.461	1.463
Si[4]	$4.14 + 0.03\mathrm{i}$	$4.38 + 0.05\mathrm{i}$

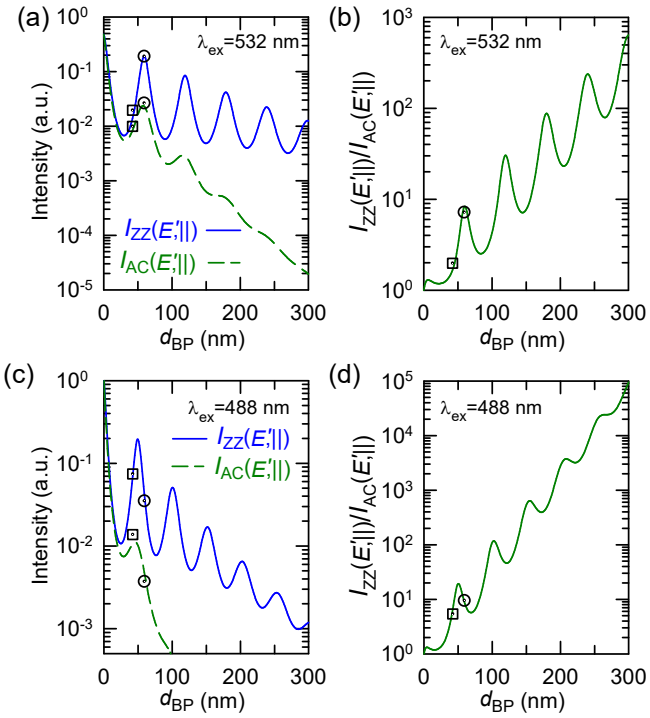

Figure S1: (a,c) $I_{ZZ}(E', \|)$, $I_{AC}(E', \|)$ and (b,d) $I_{ZZ}(E', \|)/I_{AC}(E', \|)$ of the 1LM constituent in BP/1LM deposited on 90nm-SiO_2/Si substrate as a function of d_{BP}. (a,b) λ_{ex}=532 nm, (c,d) 488 nm, respectively. Open circles and squares denote normalized Raman intensities of the 1LM component in 59 nm-BP/1LM and 42 nm-BP/1LM heterostructures, respectively.

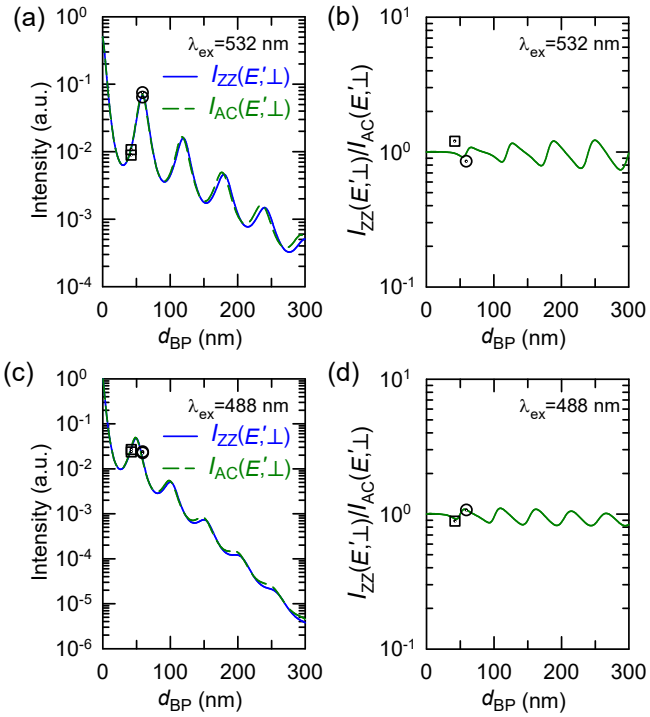

Figure S2: (a,c) $I_{ZZ}(E', \perp)$, $I_{AC}(E', \perp)$ and (b,d) $I_{ZZ}(E', \perp)/I_{AC}(E', \perp)$ of the 1LM constituent in BP/1LM deposited on 90nm-SiO_2/Si substrate as a function of d_{BP}. (a,b) λ_{ex}=532 nm, (c,d) 488 nm, respectively. Open circles and squares denote normalized Raman intensities of the 1LM component in 59 nm-BP/1LM and 42 nm-BP/1LM heterostructures, respectively.

References

(1) Li, X.-L.; Qiao, X.-F.; Han, W.-P.; Lu, Y.; Tan, Q.-H.; Liu, X.-L.; Tan, P.-H. Layer number identification of intrinsic and defective multilayer graphenes by the Raman mode intensity from substrate. *Nanoscale* **2015**, *7*, 8135–8141.

(2) Xie, J.-L.; Liu, T.; Leng, Y.-C.; Mei, R.; Wu, H.; Liu, C.-K.; Wang, J.-H.; Li, Y.; Yu, X.-F.; Lin, M.-L.; Tan, P.-H. Quantitatively Predicting Angle-Resolved Polarized Raman Intensity of Anisotropic Layered Materials. *Advanced Materials* **2025**, *37*, 2506241.

(3) Ermolaev, G. A.; Stebunov, Y. V.; Vyshnevyy, A. A.; Tatarkin, D. E.; Yakubovsky, D. I.; Novikov, S. M.; Baranov, D. G.; Shegai, T.; Nikitin, A. Y.; Arsenin, A. V.; Volkov, V. S.

Broadband optical properties of monolayer and bulk MoS_2. *npj 2D Mater. Appl.* **2020**, *4*, 21.

(4) Palik, E. D. *Handbook of optical constants of solids*, 2nd ed.; Academic Press: San Diego, 1998.